

## Chapter 2

# Experimental Realization of One-Dimensional Bose Gases

In this chapter we review the basic concepts necessary for the realization of a degenerate 1D Bose gas, as well as the actual experimental implementation of these concepts.

### 2.1 Magnetic Trapping of Ultracold Atoms

In order to achieve a 1D system of ultracold atoms, it is necessary to confine atoms very strongly in two directions. To date, two well-established techniques exist to realize such a strong confinement: optical lattices [1–3] and micro-traps [4, 5]. As discussed in the previous chapter, we aim to study single realizations of 1D Bose gases to have direct access to their intrinsic fluctuations. While optical lattices typically allow the realization of many slightly different copies in parallel, micro-traps are ideally suited to prepare and manipulate single realizations. In the following, we theoretically introduce the basic working principles of magnetic micro-traps that are realized using an atom chip. We then present the experimental apparatus to realize 1D Bose gases.

#### 2.1.1 Magnetic Trapping

An atom with angular momentum  $\mathbf{F}$  exhibits a magnetic moment  $\boldsymbol{\mu} = -g_F\mu_B\mathbf{F}$ , where  $g_F$  is the Landé g-Factor,  $\mu_B$  is the Bohr magneton. If a weak magnetic field  $\mathbf{B}$  is present, the Zeeman effect causes a linear shift of the atomic energy levels, which is given by

$$V(\mathbf{r}) = -\boldsymbol{\mu} \cdot \mathbf{B}(\mathbf{r}) = m_F g_F \mu_B B(\mathbf{r}). \quad (2.1)$$

If the magnitude  $B = |\mathbf{B}|$  of the field varies slowly enough such that  $dB/dt < \omega_L B$  is fulfilled, the atoms will adiabatically follow the shift of the Zeeman levels.

Here,  $\omega_L = m_F g_F \mu_B B / \hbar$  is the Larmor frequency of the atoms. Depending on the value of the magnetic quantum number  $m_F$  and the g-factor  $g_F$  of the atomic state, this will either lead to an attraction of the atom towards regions of lower magnetic field or to an attraction towards regions of higher magnetic field. Correspondingly, atomic states where  $g_F m_F > 0$ , are called low-field seeking states and states where  $g_F m_F < 0$  are called high-field seeking states. As Maxwell's equations forbid local maxima for static magnetic fields, only low-field seeking states can be trapped in a purely magnetic trap [6].

The most basic form of a magnetic trapping potential can be created by using a 3D quadrupole field. In the center of the quadrupole configuration the magnetic field vanishes, forming a trap for atoms in low-field seeking states. This field configuration can, for example, be realized using a pair of coils in anti-Helmholtz configuration. While this method is very efficient for the trapping of hot atoms, problems arise when the atoms are cooled down. The reason for this is that when the atoms get colder, the probability to find them at the position of zero magnetic field in the center of the trap increases drastically [7]. If the magnetic field vanishes, the adiabatic approximation introduced above is not valid anymore, the spin of the atoms can flip and they end up in an untrapped state. These so-called Majorana losses make it impossible to obtain a Bose-Einstein condensate of alkali atoms in a pure quadrupole trap [8].

The magnetic field zero in the center of the trap can be removed by adding an additional homogeneous bias field. The most common implementation of this enhanced trap is the Ioffe trap, where the quadrupole is created by four bars and the homogeneous offset field is created by two coils perpendicular to these bars. This realizes a trap with approximately harmonic confinement in all three spatial directions [6, 9].

### 2.1.2 Atom Chips

In typical experiments, macroscopic conductors are employed to create the fields that are used to trap the atoms. This has the disadvantage that the atoms usually have to be trapped far from these structures. As the magnetic field of a conductor decreases with distance, high currents are needed to create sizable field strengths. This makes experimental setups complex and difficult to handle. An alternative approach are magnetic micro-traps, where the atoms are intentionally trapped close to microscopic, current carrying structures. Micro-fabrication allows the routine creation of such structures on substrates, reaching nanometer sizes. In analogy to computer chips these devices are called atom chips. The scale reduction that is achieved by trapping the atoms close to the surface of such chips, facilitates the creation of very tight and robust traps with moderate currents. This enables the realization of compact and flexible setups, which allow for a large range of complex trap geometries [10–14], with applications ranging from atom interferometry [15, 16] and the study of gases in reduced dimensions [5, 17, 18] to quantum information processing [19–21].

The most simple of such traps, the so-called wire guide, can be formed by using a single wire and a perpendicular bias field. This situation is depicted in Fig. 2.1a. The

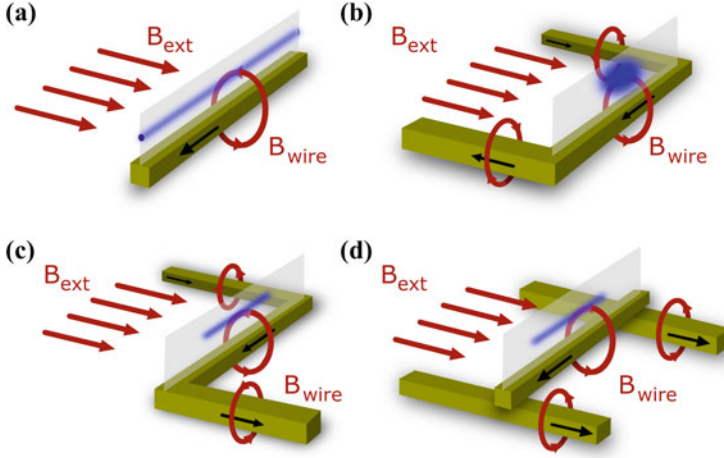


**Fig. 2.1** Different geometries to trap atoms using wires. The trapping volume is indicated in blue. **a** A wire guide, formed using a single straight wire and a perpendicular magnetic field. This results in a 2D quadrupole potential above the wire, as detailed in Fig. 2.2. **b** A U-trap, realizing a 3D quadrupole potential above the central segment of the wire. **c** The Z-trap combines the 2D quadrupole confinement of the wire guide with longitudinal confinement that is created using the bend segments of the wire. **d** Independently tunable longitudinal confinement can be realized by adding more wires

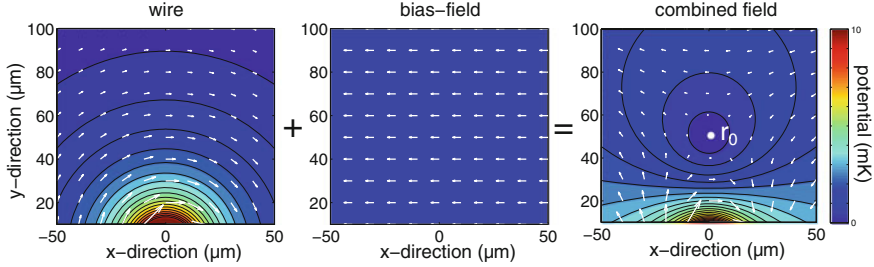


**Fig. 2.2** Magnetic field of a wire guide. A current flowing through a wire (in  $z$ -direction) creates a circular magnetic field around the wire. A homogeneous bias field is added perpendicular to the wire. At a distance  $r_0$  from the wire, the two fields cancel, creating a zero in the magnetic field which can be used to trap atoms in low-field seeking states. Figure adapted from [22]

corresponding field configuration is shown in Fig. 2.2. The bias field  $\mathbf{B}_{\text{Bias}} = B_0 \hat{\mathbf{e}}_x$  in  $x$ -direction exactly cancels the circular magnetic field  $\mathbf{B} = \mu_0 I / (2\pi r) \hat{\mathbf{e}}_r$  of the wire at a distance

$$r_0 = \frac{\mu_0}{2\pi} \frac{I}{B_0} \quad (2.2)$$

from the wire. The superposition of these fields forms a two-dimensional quadrupole field around the point of vanishing magnetic field. Here,  $I$  is the current flowing

through the wire and  $\mu_0 = 4\pi \times 10^7 \text{ Vs/(Am)}$  denotes the vacuum permeability.  $\hat{e}_r$  and  $\hat{e}_x$  denote unit vectors in the radial and  $x$ -direction, respectively.

The quadrupole field results in a force that confines the atoms in the plane perpendicular to the wire. To confine the atoms also in the third direction the trapping wire can be bend in a U-shape (Fig. 2.1b). This approximately realizes a three-dimensional quadrupole potential located above the central wire segment, which can be further optimized by flattening this part of the wire [23]. This trap configuration, in combination with appropriate laser light, is well-suited to create a magneto-optical trap close to the wires [14].

Bending the wire in a Z-shape closes the trap also in the direction along the wire (Fig. 2.1c). This realizes a trapping potential which is equivalent to that of a Ioffe-Pritchard trap [9]. An additional homogeneous bias field  $B_z$  in the  $z$ -direction allows the tuning of the field minimum to avoid Majorana losses. In the center, this trap can be very well approximated by an harmonic confinement in all three spatial directions.

More flexible trap shapes can be created by combining the single wire waveguide with additional wires. Adding wires perpendicular to the main trapping wire, as depicted in Fig. 2.1d, leads to a trap that is similar to the Z-trap. It has the advantage that the longitudinal confinement can be tuned with very little influence on the radial confinement. An equivalent configuration that avoids the necessity of wires to cross, is realized by sets of U-shaped wires next to the main trapping wire.

Our experiment includes a variety of wire arrangements to realize these different trapping configurations. In the experimental setup both macroscopic wire structures and micro-fabricated wires on an atom chip are employed. The setup will be presented in detail in Sect. 2.3. Note that in the simple examples discussed in this section, we have assumed infinitely thin wires. However, for the experiments presented in this thesis, a precise knowledge of the trapping potential created by realistic, extended wires is necessary. This situation and its detailed simulation are discussed in Appendix A.

## 2.2 Theory of Radio-Frequency Dressed-State Potentials

One particular advantage of atom chips is that they enable the creation of trapping potentials that go beyond what is possible with simple static magnetic fields. For example, a wide range of potentials can be created using near-field radio-frequency (RF) fields [24–26]. These potentials are based on the dressed-state formalism which is well known from cavity QED, where it describes the interaction of atoms with a light-field. Analyzing the interaction of the atoms with the RF radiation in a similar way, one finds new dressed eigenstates, which are superpositions of the original Zeeman levels [27–29]. If the RF radiation is turned on adiabatically, the atoms follow these new eigenstates of the system. As the dressed level structure is widely tunable via the properties of the radiation, this leads to a great flexibility in the design of the trapping geometry.

### 2.2.1 A Double-Well Potential for Ultracold Atoms

To calculate the effect of the RF dressing, we start with the semi-classical Hamiltonian of an atom in a time-dependent magnetic field

$$H = \frac{\mathbf{p}^2}{2m} + g_F \mu_B \mathbf{F} \cdot \mathbf{B}(\mathbf{r}, t). \quad (2.3)$$

The magnetic field  $\mathbf{B}(\mathbf{r}, t)$  can be separated into a part  $\mathbf{B}_S(\mathbf{r})$  which realizes the static trap for the atoms, and additional, rapidly oscillating terms  $\mathbf{B}_{\text{RF}}(\mathbf{r}, t)$

$$\begin{aligned} \mathbf{B}(\mathbf{r}, t) &= \mathbf{B}_S(\mathbf{r}) + \mathbf{B}_{\text{RF}}(\mathbf{r}, t) \\ &= \mathbf{B}_S(\mathbf{r}) + \sum_n \mathbf{B}_{\text{RF},n}(\mathbf{r}) \cos(\omega_{\text{RF}} t - \delta_n), \end{aligned} \quad (2.4)$$

with  $\delta_n$  denoting the phase offsets between the oscillating fields. Note that we assume the same frequency  $\omega_{\text{RF}}$  for all RF fields. To diagonalize this Hamiltonian, one transfers the problem into a local coordinate system where the static field  $\mathbf{B}_S(\mathbf{r})$  defines the quantization direction at every point  $\mathbf{r}$ . Subsequently, one applies the rotating-wave approximation (RWA) [26, 30], resulting in the Hamiltonian

$$\hat{H}_{\text{RWA,final}} = \frac{\mathbf{p}^2}{2m} + g_F \mu_B \mathbf{F} \cdot \mathbf{B}_{\text{eff}}(\mathbf{r}) \quad (2.5)$$

$$= \frac{\mathbf{p}^2}{2m} + g_F \mu_B |\mathbf{B}_{\text{eff}}(\mathbf{r})| F_z = \frac{\mathbf{p}^2}{2m} + V_{\text{ad}}(\mathbf{r}). \quad (2.6)$$

Equation 2.6 describes the motion of a particle in an effective magnetic field given by

$$\mathbf{B}_{\text{eff}}(\mathbf{r}) = \left( \frac{|B_{\text{RF},\perp}|}{2}, 0, |\mathbf{B}_S(\mathbf{r})| - \frac{\hbar\omega}{\mu_B |g_F|} \right)^T. \quad (2.7)$$

Here,  $B_{\text{RF},\perp}(\mathbf{r}, t)$  is the component of the RF fields that is perpendicular to the static field. This field is not a real magnetic field and thus does not have to fulfill Maxwell's equations. For this reason, it enables the creation of trapping potentials that are not possible using static fields alone. In general, the effective field is the sum of the single RF fields projected onto some direction in the xy-plane. For the  $n$ th field, this direction is defined by the angle  $\gamma_n = -g_F \delta_n / |g_F|$ . This dependence of the effective field on the sign of the g-factor makes the potentials state- and also species-selective [26].

The resulting adiabatic potential in Eq. 2.6 is given by

$$\begin{aligned} V_{\text{ad}}(\mathbf{r}) &= \tilde{m}_F g_F \mu_B \sqrt{\Delta(\mathbf{r})^2 + \Omega(\mathbf{r}, \delta)^2} \\ &= \tilde{m}_F g_F \mu_B \sqrt{\left( |\mathbf{B}_S(\mathbf{r})| - \frac{\hbar \omega_{\text{RF}}}{\mu_B |g_F|} \right)^2 + \left( \frac{B_{\text{RF}\perp}}{2} \right)^2}, \end{aligned} \quad (2.8)$$

with  $\tilde{m}_F$  being defined along the local magnetic field component  $B_{\text{eff},z}$ . The new atomic states  $\tilde{m}_F$  are superpositions of the bare  $m_F$  states. If the RF radiation is switched on slowly, the atoms adiabatically follow the new dressed states, such that atoms in a state with quantum number  $m_F$  are transferred into the corresponding state with the quantum number  $\tilde{m}_F$ .

The detuning  $\Delta(\mathbf{r})$  in Eq. 2.8 is the difference between the absolute value of the local static field and the RF frequency. The Rabi-frequency or coupling strength  $\Omega(\mathbf{r})$  defines the local coupling between the different  $\tilde{m}_F$  levels. If  $\Delta$  vanishes, it is responsible for a level repulsion and thus an avoided crossing of the levels. In this situation it acts also as an effective Ioffe field preventing Majorana losses. The fact that the coupling term defines the minima of the potential is an essential feature of the RF potentials, because by shaping its spatial dependence many different trapping geometries can be realized.

With Eq. 2.8, the calculation of the RF potentials reduces to the calculation of the perpendicular part  $B_{\text{RF}\perp}$  of the RF fields. Details of this calculation in various trapping geometries can be found in Refs. [24, 26, 29–31]. For example, using a single linear polarized RF field, as it can be realized using the near-field radiation of a single wire, two terms contribute to the adiabatic potential. Neglecting longitudinal confinement and assuming a static quadrupole field in the radial direction, the contribution from the detuning vanishes along the ring where the dressing frequency exactly corresponds to the (radially symmetric) absolute value of the static field. Along this minimum, the only contribution to the effective potential is the coupling term  $\Omega \sim B_{\text{RF}\perp}$ . As  $|B_{\text{RF}\perp}| \sim |\mathbf{B}_S \times \mathbf{B}_{\text{RF}}|$ , the coupling term becomes minimal when  $B_{\text{RF}}$  and  $B_S$  are parallel or anti-parallel. The result is a double well, where the potential minima are located opposite to each other on the ring. This situation is depicted in Fig. 2.3.

For the case of negative detuning  $\Delta$  there will always be a double well. For the case of positive detuning, which is the one usually encountered in our experiments, there will be a splitting once a critical field amplitude  $B_c = 2\sqrt{B_I \Delta}$  is reached, with  $B_I$  the Ioffe field of the static trap. The reason behind this are the different gradients of the detuning and the coupling term. This is the second way to make the potentials state- and species-selective. For example, the RF transitions in  $^{40}\text{K}$  and  $^{87}\text{Rb}$  have different frequencies, thus for a given RF frequency they will experience a different detuning. If the frequency is chosen in the correct way, only one species is split while the other remains unsplit.

More flexibility can be achieved using two linearly polarized RF fields. To obtain the resulting total RF field, the two individual fields have to be added vectorially. For example, with the appropriate phase offset, the sum of the two fields can be

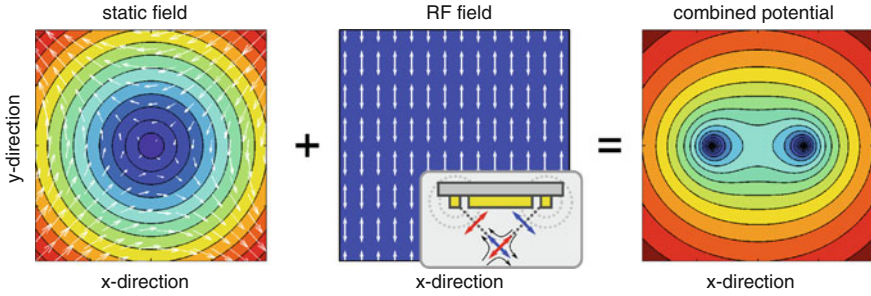


**Fig. 2.3** Creation of a horizontal double-well potential. The static trapping fields form a quadrupole potential in the  $xy$ -plane. *Arrows* indicate the local direction of the field. The RF field is linearly polarized along the  $y$ -direction. As shown in the *inset*, this polarization can, for example, be achieved by combining the RF fields of two wires with a  $\pi$  phase shift. The resulting dressed-state potential exhibits two minima at the positions where the static and the RF field are parallel. Rotating the linear polarization of the RF field leads to a rotation of the double well

made linearly polarized in the horizontal or in the vertical direction, which changes the orientation of the double well accordingly. In our setup with two RF wires, we employ currents with a phase shift of  $\delta = \pi$  to realize the vertical polarization that forms a horizontal double well. Rotating the double well in arbitrary directions is possible by using different amplitudes for the two RF fields.

Further trapping geometries can be realized using circular or elliptical polarizations. For example, circular polarization ( $\delta = \pi/2$ ) leads to a ring shaped trap, where the atoms explore a 2D surface with periodic boundary condition. Elliptical polarization, on the other hand is well-suited to create state- and species-dependent potentials [31].

### 2.2.2 Beyond the Rotating-Wave Approximation

For  $^{87}\text{Rb}$  in the  $F = 2$  state, the dressing within the RWA turns five bare  $m_F$  states into five dressed  $\tilde{m}_F$  states. However, in a diagonalization of the full Hamiltonian (Eq. 2.3), many more of these manifolds, each containing five  $\tilde{m}_F$  states appear (see Appendix A and Refs. [29, 32, 33]). A quantum mechanical analysis reveals that every manifold can be associated with a fixed, but large number of photons in the RF field. Adjacent manifolds are therefore separated by the energy  $\hbar\omega_{\text{RF}}$  of a single RF photon. This is in complete analogy to the analysis of dressed states in cavity QED [27].

The full diagonalization shows that the rotating-wave approximation provides a good approximation of the dressed-state level structure as long as

$$\Omega, \Delta \ll \omega. \quad (2.9)$$

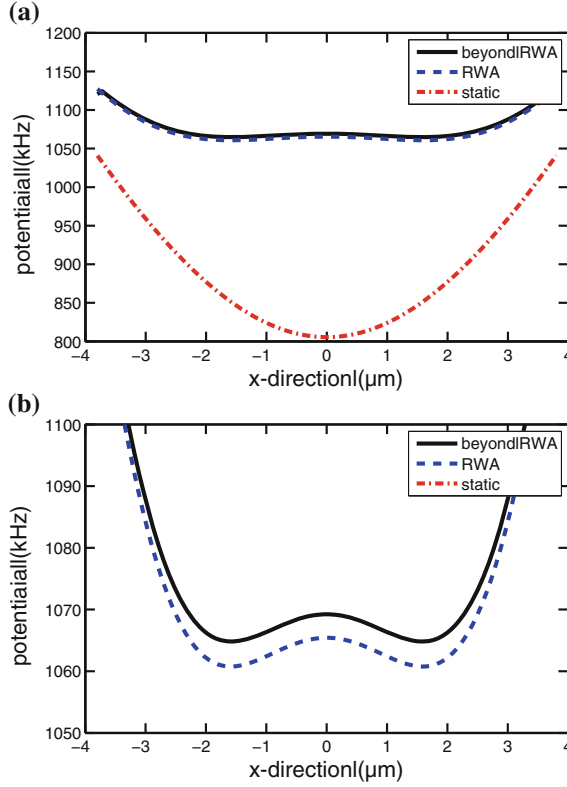


**Fig. 2.4** Typical trapping potentials. Simulated trapping potentials for the static fields as well as the RF fields in a rotating-wave approximation (RWA) calculation and a beyond RWA calculation. **a** The RF dressing shifts the static level up in energy, forming the dressed double well. **b** Zoom into the double-well potential, revealing the differences between RWA and beyond RWA calculation. Parameters of the double well, such as barrier height or the distance between the two wells can be tuned using the applied RF radiation. Here, the RF current is  $I_{\text{RF}} = 20$  mA and the detuning from the  $m_F = 2 \rightarrow m_F = 1$  transition is 30 kHz. The static trap is located  $100 \mu\text{m}$  from the chip surface. For details on the choice of parameters, see Chap. 4

Here,  $\omega$  is the atomic transition frequency between the bare  $m_F$  states. This condition can be understood from the fact that the dressed  $\tilde{m}_F$  states in each manifold are separated by an energy  $\hbar\tilde{\omega} = \hbar\sqrt{\Delta^2 + \Omega^2}$ , which remains smaller than the separation of different manifolds as long as Eq. 2.9 is fulfilled. If this is not the case, different manifolds overlap and it is not possible to analyze them separately anymore.

The atom chip easily enables couplings  $\Omega$  which are much larger than  $\omega$ , violating the condition in Eq. 2.9. Moreover, the detuning can locally become on the order of  $\omega$ . To obtain a precise description of the potentials in these cases therefore requires the diagonalization of the full Hamiltonian. Exemplary results are presented in Fig. 2.4.



Labeling the  $\tilde{m}_F$  manifolds with the index  $\kappa$ , off-resonant contributions from the overlap of the different manifolds lead to many possible transitions between the dressed states. These transitions can be summarized by the resonance condition

$$\omega_{\text{res}} = \Delta\kappa \omega_{\text{RF}} + \Delta\tilde{m}_F \tilde{\omega}, \quad (2.10)$$

Here,  $\omega_{\text{RF}}$  is the frequency of the RF radiation and  $\hbar\tilde{\omega}$  denotes the energy difference between the  $\tilde{m}_F$  states of a single manifold. The selection rules for these transitions are given by  $\Delta\kappa = 0, \pm 1, \pm 2, \dots$  and  $\Delta\tilde{m}_F = \pm 1$ .

### 2.3 Experimental Setup and Cooling Sequence

This chapter describes the experimental realization of a 1D quantum gas of bosonic  $^{87}\text{Rb}$  atoms on an atom chip.

The setup consists of two vacuum chambers, a design widely used in many cold atom experiments. In principle, the fast cooling cycles on an atom chip also allow for single chamber designs. The two chamber setup was chosen to allow also for multi-species experiments with fermionic  $^{40}\text{K}$  or bosonic  $^{39}\text{K}$ . The first chamber is used as an efficient source for cold atoms, which are then transferred to the second science chamber where the actual experiments take place. Details of the design are described in [31, 34, 35]. An overview is depicted in Fig. 2.5.

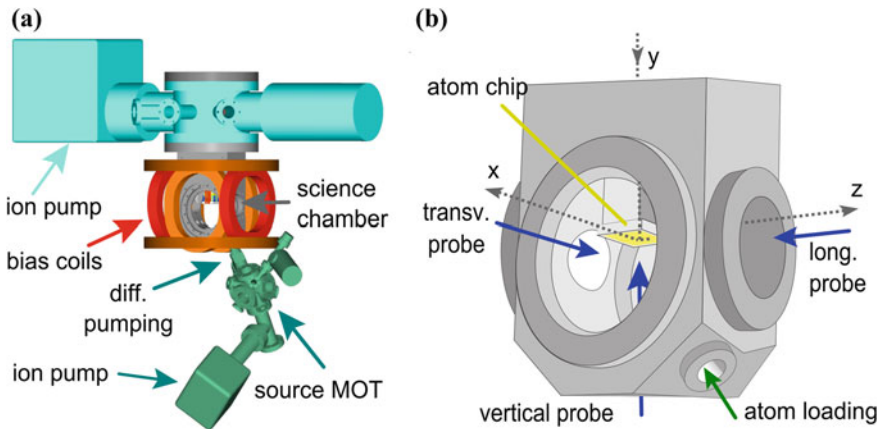


**Fig. 2.5** Experimental setup. **a** Source-MOT and science chamber with the vacuum system [34]. The two chambers are connected by a differential pumping stage. A resonant push beam is used to transfer the atoms from a 3D source-MOT in the lower chamber to a mirror-MOT in the science chamber. The setup is designed such that it allows for good optical access to the science chamber from all directions. **b** Close-up of the science chamber with the atom chip mounted upside down in the center [37]. Large windows enable absorption imaging in all three spatial directions

In the course of this thesis, the first degenerate Bose gases of  $^{87}\text{Rb}$  were realized in the new machine. In the following we present a short summary of the typical experimental procedure. Details can be found in Refs. [22, 36].

### 2.3.1 Atom Source and Precooling

The experimental cycle starts with a source of cold atoms. The source consists of a 3D magneto-optical (3DMOT) trap that is created in a stainless steel chamber with six CF40 and eight CF16 flanges. The chamber houses commercial rubidium dispensers<sup>1</sup> which are continuously operated at a current of 7.5 A to achieve a high Rb background pressure. One CF40 flange is connected to an ion pump,<sup>2</sup> resulting in a typical pressure of  $10^{-8}$  mBar. The 3DMOT uses a six-beam configuration, where the lasers are detuned by 22 Mhz from the  $F = 2 \rightarrow F' = 3$  transition of the  $^{87}\text{Rb}$   $D_2$  line ( $\lambda_{D2} \sim 780$  nm). The laser power of 15 mW per beam is derived from a single cooling laser,<sup>3</sup> which also provides most of the other light used in the experiment. Additional repumping light on the  $F = 1 \rightarrow F = 2$  transition is derived from a home-built diode laser system. During the operation of the source-MOT a resonant pushbeam is used to continuously transfer atoms into the science chamber through a differential pumping stage.

### 2.3.2 Science Chamber and Mirror Magneto-optical Trap

The science chamber has a size of  $25 \times 16 \times 9$  cm and is produced from a single block of stainless steel (Fig. 2.5b). It is pumped by an ion pump,<sup>4</sup> resulting in a typical pressure of  $10^{-10}$ – $10^{-11}$  mBar. Additional pumping can be provided using a titanium sublimation pump. The main feature of the science chamber are two 100 mm diameter windows which allow for good optical access in what later will be the transversal direction of the 1D gases. Further view ports on all other sides of the chamber allow for additional optical access in all other directions. The chamber is surrounded by large bias coils in all three spatial directions. The micro-fabricated atom chip is mounted upside down in the center of the chamber. Several macroscopic copper structures are located behind the actual atom chip and are used for additional trapping and cooling. The first of these is a U-shaped structure which, together with an external magnetic bias field, creates a quadrupole field that is centered less than 1 cm away from the chip surface. This quadrupole field and four laser beams are used to create a second MOT. To this end, two of the laser

---

<sup>1</sup>SEAS Getter, Inc.

<sup>2</sup>Varian 201/s Star-Cell.

<sup>3</sup>Coherent MBR 110 Ti:Sa laser, pumped by a Coherent Verdi V18, output 1.2 W @ 780 nm.

<sup>4</sup>Varian 150 l/s Star-Cell.

beams are reflected from the atom chip's highly reflective surface under an angle of  $45^\circ$ . This represents a mirror-MOT which is equivalent to the usual six-beam MOT configuration [14, 23]. Typical powers per beam are 20 mW. The light for the cooling, as well as for additional repumping is derived from the same lasers as for the source-MOT. The mirror-MOT is continuously loaded for 10 s using the push beam from the lower chamber.

### 2.3.3 Wire Traps and Evaporative Cooling

In the next step, the atoms are transferred to a first magnetic trap formed by two Z-shaped copper structures with cross-sections of  $(1 \times 1) \text{ mm}^2$  and  $(2 \times 1) \text{ mm}^2$ , which are located behind the chip. To this end, we first compress the mirror-MOT by increasing the bias fields. This prepares the MOT for a good mode-matching with the magnetic trap. Subsequently, all magnetic fields are turned off and a 8 ms long stage of sub-Doppler cooling in an optical molassis is used to decrease the temperature of the atoms. This yields  $10^8$  atoms at temperatures around  $50 \mu\text{K}$ . The optical molassis is followed by a 1 ms pulse of  $\sigma^+$  light on the  $F = 2 \rightarrow F' = 2$  transition to optically pump the atoms into the trappable  $F = 2, m_F = 2$  state. We then ramp up a current of (60–70) A in both copper structures to form a trap that has a depth of approximately 1.6 mK and estimated trap frequencies of  $\omega_z = 2\pi \times 17 \text{ Hz}$  and  $\omega_\perp = 2\pi \times 50 \text{ Hz}$ . At this point,  $7 \times 10^7$  atoms are trapped, corresponding to a transfer efficiency of about 70 % from the MOT. This number depends critically on the efficiency of the optical pumping. The current in the larger Z-structure is subsequently ramped down within 350 ms, followed by a 2 s compression of the Z-trap. This results in a trap which is characterized by  $\omega_z \sim 2\pi \times 24 \text{ Hz}$  and  $\omega_\perp \sim 2\pi \times 800 \text{ Hz}$ . Subsequently, evaporative cooling is initiated by applying RF radiation via the U-shaped structure. The radiation is created using an arbitrary wave-form generator.<sup>5</sup> Typical coupling strengths of the RF are (2–6) kHz. Starting from a frequency of around 15 MHz, we decrease the frequency of the RF radiation roughly exponentially to 0.75 MHz within 6.1 s. This increases the phase space density close to unity, with a temperature of about  $10 \mu\text{K}$  and  $10^6$  atoms.

### 2.3.4 The Atom Chip

Typically the cold cloud in the macroscopic trap is not cooled further to quantum degeneracy, but transferred to the microscopic traps on the atom chip. To this end we linearly ramp up the current in the chip structures within 500 ms, while in the mean time decreasing the current in the macroscopic Z-structure. This allows for a nearly

---

<sup>5</sup>Tabor Electronics WW1071.

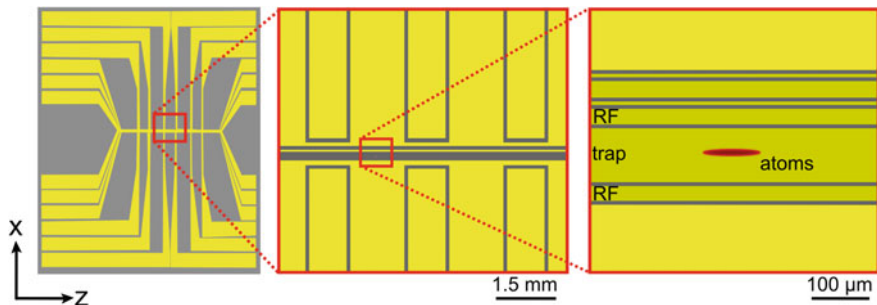


**Fig. 2.6** Layout of the atom chip. The atom chip consists of approximately  $1.2\ \mu\text{m}$  thick, single layer gold structures that have been evaporated on a  $35.7 \times 0.525 \times 29.7\ \text{mm}$  sized silicon substrate by means of photo lithography. Six wires of different widths are available to realize variable trapping geometries for the atoms. For the experiments presented this thesis, we use a  $100\ \mu\text{m}$  wire together with external bias fields to create the static trapping potential. Tunable longitudinal confinement is realized using 4 of the 6  $100\ \mu\text{m}$  wide U-shaped wires. Two parallel  $30\ \mu\text{m}$  wide wires adjacent to the main trapping wire are used to apply radio frequency fields. A detailed description of the design and the fabrication process can be found in [31]

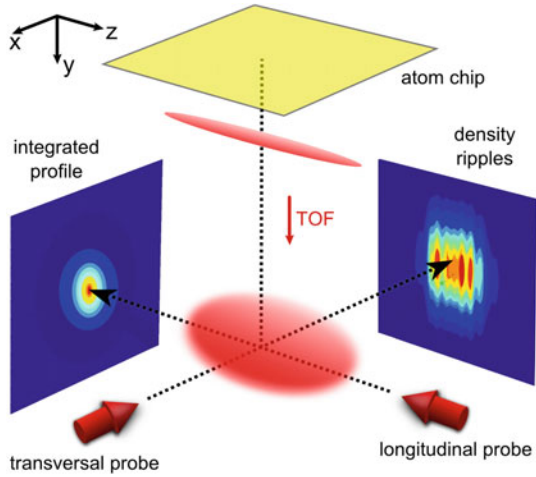
loss-less transfer of the atoms to the chip, much better than what could be achieved by loading the chip directly from the large volume mirror-MOT.

The atom chip employed is a single layer gold chip fabricated on a silicon substrate.<sup>6</sup> The wire layout is shown in Fig. 2.6. It allows for a large variety of traps, formed using  $100$  or  $30\ \mu\text{m}$  wide main trapping wires, in conjunction with external bias fields. Each of the trapping wires is combined with two additional smaller parallel wires, which are used for RF manipulation of the atoms. Flexible longitudinal trapping is created using 6 U-shaped wire structures.

After transferring the atoms to the chip, further evaporative cooling is performed. For the experiments presented in this thesis, we typically employ a trap formed using the  $100\ \mu\text{m}$  wide main trapping wire and two neighboring pairs of U-structures. Typical currents are  $810\ \text{mA}$  in the  $100\ \mu\text{m}$  wire and  $295\ \text{mA}$  in each of the U-structures. To minimize fluctuations, the chip currents are supplied by car batteries. A bias field in  $x$ -direction is used to set the properties of the trap. It ranges from  $12$  to  $16\ \text{G}$ , realizing a trap located between  $120$  and  $90\ \mu\text{m}$  below the chip surface, with radial trapping frequencies of  $\omega_{\perp} = 2\pi \times (1.4\text{--}2.5)\ \text{kHz}$ . The longitudinal trapping frequency is  $\omega_z = 2\pi \times (7\text{--}12)\ \text{Hz}$ . Further evaporative cooling in this trap leads to degenerate gases with temperatures in the range of  $(20\text{--}200)\ \text{nK}$ , and containing  $10^3\text{--}10^4$  atoms. This realizes a single 1D Bose gas that can be further manipulated in the experiments.

<sup>6</sup>Produced by M. Trinker at Zentrum für Mikro- und Nanostrukturen (ZMNS) of TU Wien.

**Fig. 2.7** Imaging setup for a single 1D Bose gas. A cloud of phase fluctuating 1D bosons is prepared below the atom chip. Upon its release it falls under gravity and expands in time-of-flight (TOF). The cloud can be illuminated transversally to obtain an image of the density ripples that form in expansion, or longitudinally, to obtain an integrated image of the atomic density profile. Figure adapted from [22]



### 2.3.5 Imaging Systems

Independent of the particular experiment that is performed, information is always extracted using standard absorption imaging [9]. After rapidly turning off all trapping potentials, the atoms fall under gravity and expand for a variable time-of-flight. The observation is performed using three different imaging systems, each pointing along one spatial direction. For all imaging systems, we use the  $F = 2 \rightarrow F' = 3$  transition of the  $D_2$  line of  $^{87}\text{Rb}$  with an intensity corresponding to about 10 % of the saturation intensity. The finite resolution of the imaging process can be described by a radially symmetric Gaussian point spread function [22, 38]

$$f(r) = \frac{1}{\sqrt{2\pi}\sigma_{\text{PSF}}} \exp\left(-\frac{r^2}{2\sigma_{\text{PSF}}^2}\right), \quad (2.11)$$

where  $\sigma_{\text{PSF}}$  is the width of the point spread function.

An overview of the imaging process for a single 1D Bose gas is shown in Fig. 2.7. The corresponding procedure for two gases in a double well is presented in Fig. 2.8. A detailed description of the absorption signal for each imaging system can be found in Ref. [22].

#### Longitudinal Imaging System

The longitudinal imaging records the integrated atomic density distribution along the  $y$ -direction using a standard CCD camera.<sup>7</sup> It uses a two-lens setup, resulting in a field of view of  $2.5 \times 1.67$  mm and a pixel size of  $2.45 \mu\text{m}$ . As the optical access is shared with the MOT beams, the optical setup limits the numerical aperture of this

<sup>7</sup>Andor DV435-BV-958, serial number CCD5302.

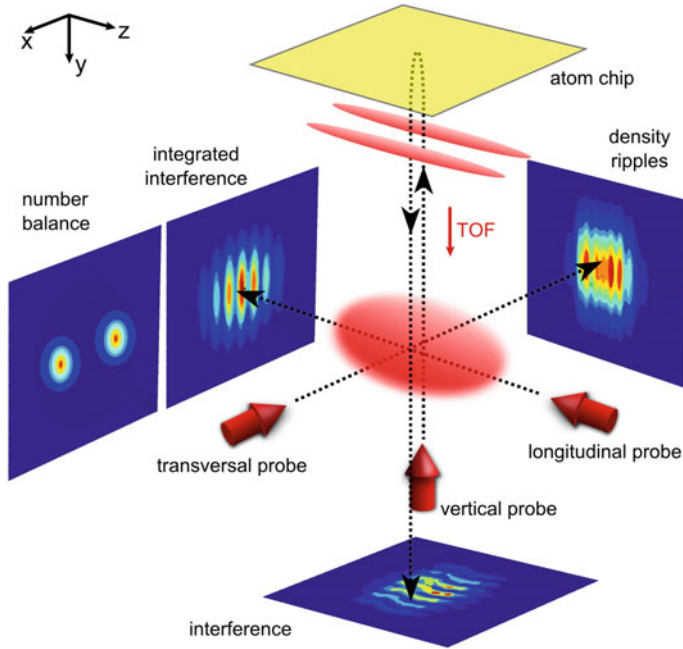


**Fig. 2.8** Imaging setup for two interfering 1D Bose gases. After turning off all trapping potentials, the clouds expand and form a matter-wave interference pattern. This pattern can be imaged using the vertical imaging, or by integration of the cloud along its longitudinal axis. As the line of sight of the vertical imaging is blocked by the atom chip, the imaging beam is reflected before passing the atoms. The transversal imaging system records the sum of the density ripples in both gases. Alternatively, the double-well trap can be turned off before the static trap (see text for details). After time-of-flight expansion (TOF), this leads to two well-separated clouds which can be individually resolved using the longitudinal imaging system. This procedure can thus be used to count the number balance of atoms in the left or right gas. Figure adapted from [22]

imaging system to approximately 0.096 [36]. The imaging system is used to record integrated pictures of interfering 1D gases. It is also used to measure the number balance of atoms trapped in a double well. Focusing is accomplished using a detuned imaging beam, which results in characteristic near-field diffraction effects [22, 39]. For example, imaging an interference pattern will result in a constant interference contrast as a function of detuning only if the imaging is focused. If it is defocused, a linear variation of the contrast with detuning can be observed.

### Transversal Imaging System

The second imaging system is used to study the atoms along their transversal direction. To benefit from the large optical access in this direction, the imaging system uses a high-resolution objective with a numerical aperture of 0.26 [40, 41]. It images

the atoms onto a standard CCD camera,<sup>8</sup> and has a field of view of  $0.7 \times 1$  mm and a pixel size of  $1.05 \mu\text{m}$  [22]. The system is optimized for high-resolution in situ imaging, but can also be used to image the density ripple patterns that form after time-of-flight expansion of a phase-fluctuating 1D Bose gas. Examples of temperature measurements based on these patterns are presented in Sect. 2.3.6. Coarse focusing is accomplished by detuning the imaging beam, fine tuning using the density ripple spectrum [42, 43]. From this density ripple spectrum, the resolution can be determined to be  $\sigma_{\text{PSF}} = (2.55 \pm 0.10) \mu\text{m}$ .

Additionally, this imaging system can be used for a high-resolution optical pumping scheme, which spatially selects subsections of clouds for the longitudinal imaging system [37, 44]. In this scheme atoms are illuminated by a beam resonant to the  $F = 2 \rightarrow F' = 1$  transition. After scattering on average only 1–2 photons they decay into the  $F = 1$  state, which renders them invisible to further imaging light on the  $F = 2 \rightarrow F' = 3$  transition. By imaging a target with variable size onto the atoms through the high-resolution objective, parts of the cloud can be protected from this state change. This scheme is used together with the longitudinal imaging to perform matter-wave interference experiments with variable integration length in Chap. 4.

Moreover, this imaging system can be easily replaced by an overview imaging system using a flip mirror. The overview imaging system has a field of view of  $4 \times 5.3$  mm, a pixel size of  $3.84 \mu\text{m}$  and uses a Pixelfly CCD camera. Due to the large field of view it is particularly useful for the calibration of the molassis and the optical pumping, where the atomic clouds are too large to be observed with the other imaging systems.

### Vertical Imaging System

The third imaging system records the atomic density distribution from below. This is of particular importance for the experiments presented in this thesis, as it enables the direct imaging of the local interference pattern of two 1D Bose gases. While imaging this interference pattern is, in principal, also possible using the optical pumping scheme presented above, the vertical imaging directly provides the full spatial information including all integration lengths at once and down to the resolution limit. It is this feature which enables the measurement of phase correlation functions, which is central to Chaps. 5 and 6.

A conventional absorption imaging setup in this direction is rendered impossible by the atom chip, which directly blocks the line of sight. This problem can be circumvented by using the chip as a mirror, before collecting the light on a electron multiplying CCD (EMCCD) camera<sup>9</sup> which is currently used without the amplification stage. The EMCCD camera was chosen to prepare this imaging system for future single-atom sensitive fluorescence imaging [45].

Special care has to be taken as the structures on the chip can severely degrade the image quality through diffraction of the light beam. Therefore, the imaging beam

<sup>8</sup>Andor DV435-BV-958, serial number CCD5303.

<sup>9</sup>Andor iXon DV887.



is focused such that only the central trapping wire is illuminated. The focus of the beam is positioned close to the atoms such that they are only illuminated once by the beam, after it has been reflected from the atom chip surface. This results in a circular field of view with a radius of about  $100\text{ }\mu\text{m}$ . The pixel size is  $2.02\text{ }\mu\text{m}$ . As for the longitudinal imaging, focusing is achieved by imaging an interference pattern with a detuned imaging beam. Note that due to the imaging beam focusing, the focal position of this imaging system is fixed and corresponds to a time-of-flight of  $15.7\text{ ms}$ . The resolution can be determined using measurements of phase correlation functions (see Sect. 2.4) and corresponds to  $\sigma_{\text{PSF}} = (3.6 \pm 0.1)\text{ }\mu\text{m}$ .

### 2.3.6 Making and Probing Degenerate Gases

The emergence of a quasi-condensate is shown in Fig. 2.9. The transversal images reveal strong density fluctuations, which become less pronounced with decreasing temperature. These density fluctuations are a direct consequence of the in situ phase fluctuations of the quasi-condensate and were first observed in elongated 3D condensates [46]. In low-dimensional gases, interactions during the expansion are negligible and thus the spectrum and the correlation properties of the density fluctuations after expansion can be calculated [47]. Interestingly, the scaling laws governing the

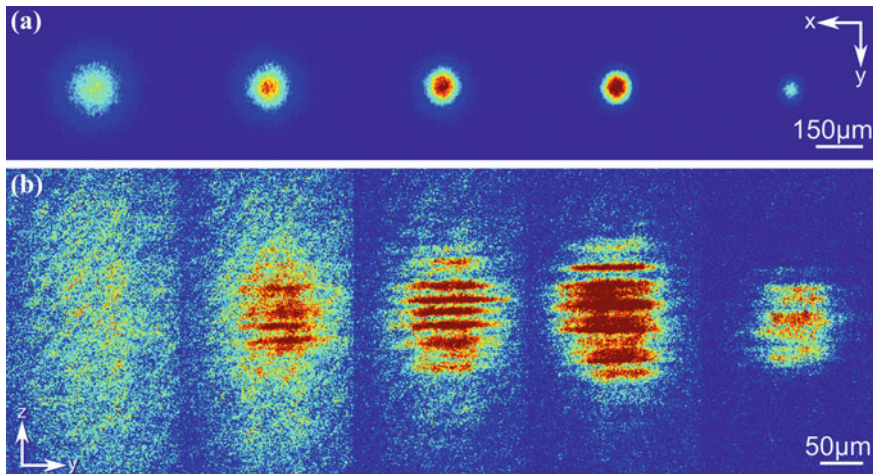


**Fig. 2.9** Emergence of a quasi-condensate. Absorption images after 12 ms time-of-flight. From left to right the final RF evaporation frequency decreases from 450 to 410 kHz in steps of 10 kHz. **a** Images using the longitudinal imaging system reveal the transition from a Gaussian thermal cloud to a strongly peaked quantum degenerate gas. **b** Images using the transversal imaging system show how density ripples slowly emerge withing the thermal background, signaling the emergence of the quasi-condensate. Decreasing the RF frequency the thermal background vanishes and the quasi-condensate grows. As temperature decreases the density ripples become less pronounced



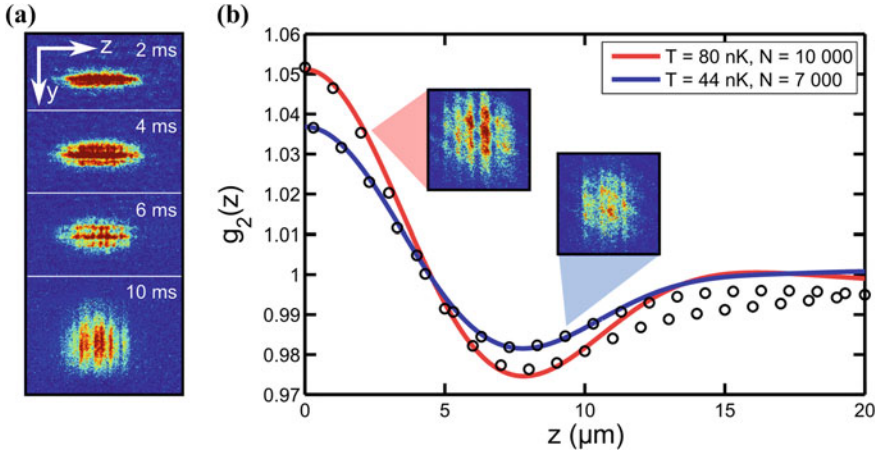


**Fig. 2.10** Thermometry using density fluctuations in expansion. **a** In situ phase fluctuations lead to density fluctuations of a quasi-condensate in time-of-flight expansion. **b** The density-density-correlation function of these fluctuations can be used for thermometry [47, 50]. If the temperature is high, phase fluctuations are strong, leading to strong density fluctuations in time-of-flight. If the temperature is low, phase fluctuations are reduced

spectra in 1D and 2D Bose gases have been predicted to be identical, a topic which is currently under intense study [42, 48, 49]. In our experiment we use the correlation properties of the density ripples to measure the temperature of the gas.

To this end the experiment is repeated approximately 100 times to extract the density-density correlation function [36, 42, 47, 50]. The result is compared to Ornstein-Uhlenbeck simulations for quasi-condensates of different temperatures to fit the temperature of the gas. Examples are presented in Fig. 2.10.

It is well known that the proximity of the atoms to the wires makes the trapping potentials on atom chips very sensitive to imperfections of the wire structures [51]. Information about the trapping potential can be obtained by using the atoms as a probe for these corrugations. To this end, cold but still thermal clouds are imaged after a short time of flight. Averaging over many realizations, structures in the density profile directly reveal deviations from a smooth trapping potential. Examples are presented in Fig. 2.11a. The overall potential closely follows a harmonic potential. In the center, small deviations can be observed which are the result of wire corrugations. These corrugations become more pronounced the closer the atoms are located to the wires. To minimize this effect we exclusively use traps which are formed at least  $100\text{ }\mu\text{m}$  from the chip.

The harmonic confinement of the trap can be further characterized using trap frequency measurements. A short step in the current of the trapping wires displaces the trap and induces collective oscillations of the atoms. Fitting position and width of the cloud after time-of-flight expansion for varying evolution times after

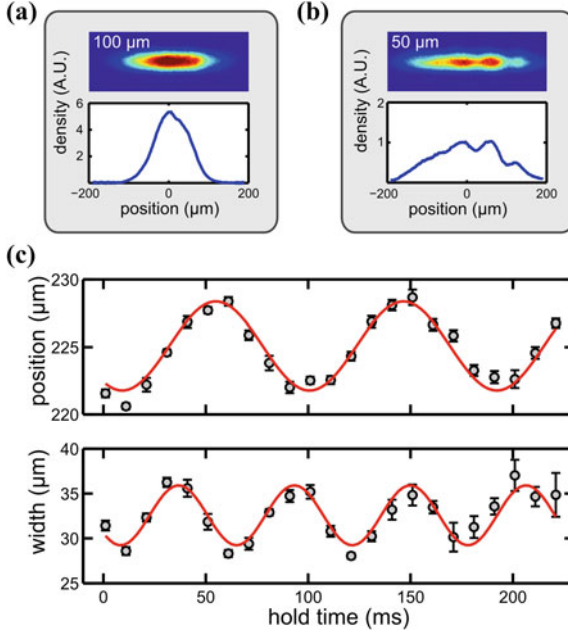


**Fig. 2.11** Characterization of the trapping potential. Wire corrugations can lead to a deformation of the potential. The effect can be probed using the density profile of thermal atoms. **a** At a distance of  $100\ \mu\text{m}$  from the chip, the integrated profile is almost smooth, corresponding to a smooth trapping potential. **b** Moving the atoms closer to the chip wire corrugations are revealed. To minimize the effect of these corrugations all experiments presented in this thesis have been performed at distances around  $100\ \mu\text{m}$  from the chip. **c** The (approximately) harmonic confinement of the trap in **(a)** is characterized using trap frequency measurements. For the trap in this example, we find frequencies of  $\omega_D = \omega_z = 2\pi \times (10.94 \pm 0.14)\ \text{Hz}$  for the collective dipole oscillations (*top*) and  $\omega_B = 2\pi \times (17.67 \pm 0.26)\ \text{Hz}$  for the collective breathing oscillations (*bottom*) of the atoms. The ratio  $\omega_B/\omega_D = 1.61 \pm 0.03$  is close to the predicted value of  $\sqrt{3}$  [52]. Similarly, the radial trapping frequency can be measured. Typical values are  $\omega_\perp = 2\pi \times (2\text{--}2.1)\ \text{kHz}$

the displacement, we obtain the frequencies of dipole and breathing oscillations, respectively. As expected for a trapped 1D Bose gas, we find a ratio close to  $\omega_B/\omega_D \sim \sqrt{3}$  [52, 53]. Exemplary results are shown in Fig. 2.11b.

## 2.4 Experiments with Atoms in a Tunable Double-Well Potential

Having produced and characterized a single harmonically trapped 1D Bose gas provides a solid starting ground for experiments in a double-well potential. In this chapter, this double-well potential is characterized. Subsequently, we introduce the

tools to probe the equilibrium state of 1D bosons in this potential via matter-wave interference.

### 2.4.1 Characterization of the Radio-Frequency Dressing

To create the dressed-state potentials we use two parallel  $30\text{ }\mu\text{m}$  wide wires adjacent to the main trapping wire. The RF radiation is provided by a two-channel arbitrary wave-form generator<sup>10</sup> which allows the individual control of both phase and amplitude in each of the wires. Typical RF currents for the creation of a double well located  $100\text{ }\mu\text{m}$  below the chip surface are  $I_{\text{RF}} = (20\text{--}25)\text{ mA}$  per wire. To characterize the applied RF fields we first monitor the 5-level Rabi oscillations in the bare state basis by mapping the populations of the different  $m_F$  states using a Stern-Gerlach experiment. To this end, we turn on the RF for a fixed time at a variable frequency. Then the trapping potentials are switched off and a field gradient is applied via one of the macroscopic Z-wires during the ensuing time-of-flight expansion. As the different  $m_F$  states have different magnetic moments they are spatially separated and can be imaged individually using the longitudinal imaging system. To fit the results, we solve the 5-level Rabi problem and find typical coupling strengths on the order of several hundred kHz.

To precisely study the dressed-state level structure we perform spectroscopy with an additional weak RF field [29]. This RF field is applied via the U-wire, as in the normal evaporative cooling sequence. It couples the different dressed states, just as it would with the bare states, leading to pronounced loss features in the atom number. The results of this RF spectroscopy are shown in Fig. 2.12. We use the position of the resonances to calibrate our simulation of the potentials (see Appendix B). Another benchmark for the simulation can be obtained by measuring the distance between the wells as a function of RF current.

The trap frequencies in the double well are characterized in the same way as in the static trap. Typically, both longitudinal and radial trap frequency are about 30 % lower than in the static trap. The exact value depends on the applied RF current and can be very well estimated using the simulation of the potentials.

### 2.4.2 Turning Off the Double Well

When loading the double well the RF can be ramped up slowly, thus transferring the atoms adiabatically from the bare states to the dressed states. This is not possible when the atoms are released from the trap, as all potentials have to be switched off immediately. The rapid change of the quantization axis leads to a decomposition of the atoms into the various bare states. This has significant implications for interference

---

<sup>10</sup>Tabor Electronics WW5062.

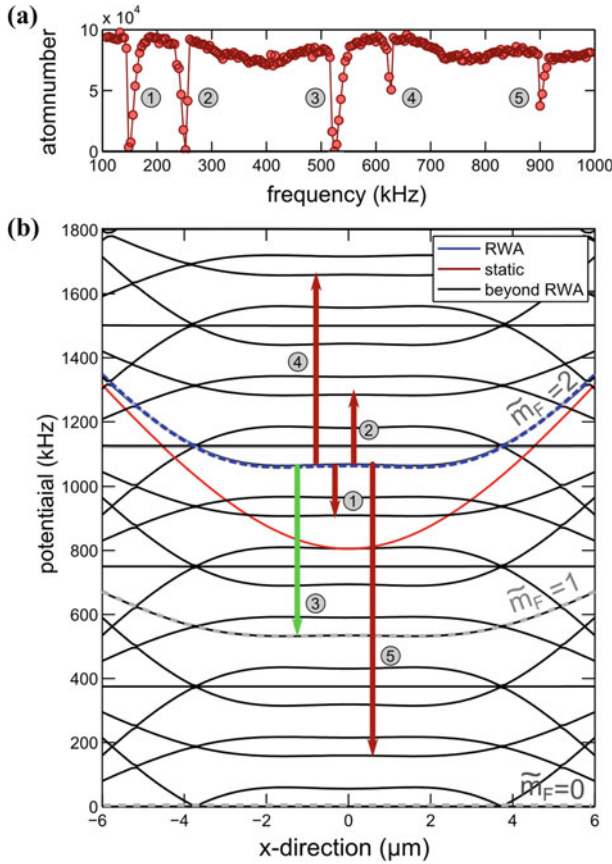
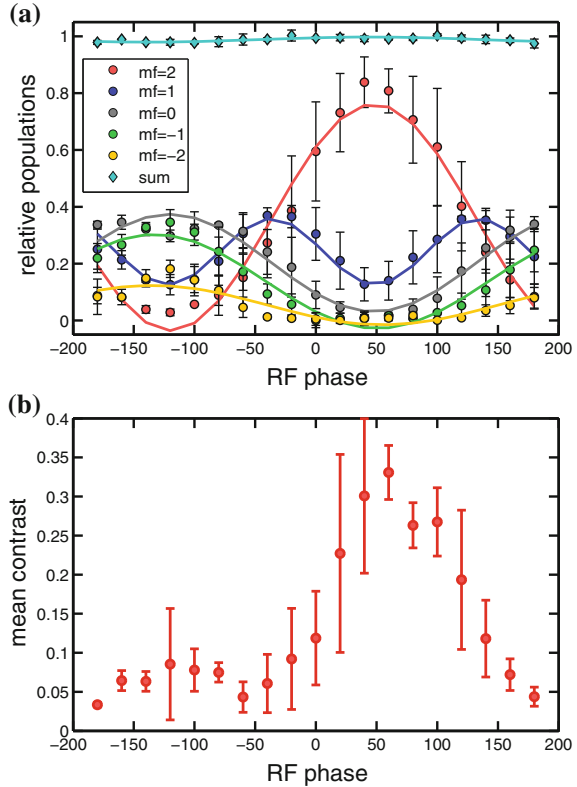


**Fig. 2.12** RF spectroscopy of the dressed states. **a** A weak additional RF field is used to outcouple atoms from the dressed trap. Resonances appear whenever the RF field is resonant with a transition between the different dressed states. **b** Simulation of the level structure in the dressed trap, which enables the identification of the transitions (1)  $\Delta\kappa = +1$ ,  $\Delta\tilde{m}_F = -1$ , (2)  $\Delta\kappa = +2$ ,  $\Delta\tilde{m}_F = -1$ , (3)  $\Delta\kappa = +0$ ,  $\Delta\tilde{m}_F = -1$ , (4)  $\Delta\kappa = +3$ ,  $\Delta\tilde{m}_F = -1$ , and (5)  $\Delta\kappa = -1$ ,  $\Delta\tilde{m}_F = -1$ . Gray dashed lines indicate the sub levels of the  $\Delta\kappa = 0$  manifold. The green line indicates transition (3), which is typically used for RF cooling in the experiments. Note that resonances (2) and (4) to states with higher energy are shifted by approximately 25 kHz because of the high temperature of the atoms used in this measurement

experiments as the different  $m_F$  states have different magnetic moments. Any small residual field during expansion will displace the different  $m_F$  states with respect to each other, leading to a decrease in interference contrast. Note that this does not change the dynamics that are observed, it just reduces the experimental sensitivity to small changes in contrast. The decomposition can be optimized by properly choosing the phase of the RF field. Typical observations are shown in Fig. 2.13. From these

**Fig. 2.13** RF potential switch-off. **a** For the ideal choice of the RF phase, most atoms are projected back into the  $m_F = 2$  bare state. *Solid lines* are a guide to the eye. **b** This leads to a maximization of the interference contrast

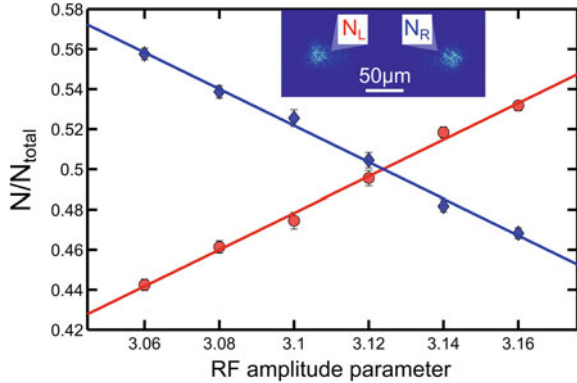


results we extract the best value for the phase, where most of the atoms are transferred into the  $m_F = 2$  bare state, resulting in the highest contrast.

### 2.4.3 Equilibrium States: Cooling into the Double Well

To prepare a pair of gases in equilibrium we change the experimental sequence and let the evaporative cooling in the static chip trap end at a frequency which is significantly higher than the one needed to create a degenerate gas. We then ramp up the RF potentials in 10 ms. As the trapping frequency is reduced during the splitting process, special care is taken not to cool the gas to degeneracy by adiabatic expansion [9]. Subsequently, the RF cooling is resumed using one of the resonances identified in the RF spectroscopy. Typically, the  $\Delta\kappa = 0$ ,  $\Delta\tilde{m}_F = -1$  resonance at approximately 520 kHz is used for 300 ms of further cooling, creating two degenerate gases in the individual double wells, which, by definition, are completely independent of each other. This is the thermal equilibrium situation of two gases in a double well.

**Fig. 2.14** Atom number imbalance. By changing the relative amplitude of the two RF currents the double well can be tilted. This leads to a mean atom number imbalance between the two wells. The imbalance can be measured by turning off the RF currents before the static currents. This leads to a separation of the two wave packets in time-of-flight (details see text)



For example, symmetric and anti-symmetric degrees of freedom exhibit the same temperatures and are thus in equilibrium.

At this point we can perform two complimentary measurements. First, to access the atom number imbalance between the two gases, the RF amplitude is ramped down over 40 periods, corresponding to a time scale of 0.1 ms. This transfers the atoms back into the bare states, while the static trapping potential is still present. As the ramp-down is fast compared to the radial trapping frequency ( $\omega_{\perp} \sim 2\pi \times 2$  kHz), the resulting two clouds are displaced from the energy minimum of the static trap. Similar to classical balls they will thus roll down the potential. Turning off the trap at the time when they reach the potential minimum prepares two clouds with opposite momenta. These momenta are large enough to separate the two clouds spatially after time-of-flight, enabling the measurement of the respective atom numbers using the longitudinal imaging system. Examples are shown in Fig. 2.14. Controllable atom number imbalances can be prepared by using a small asymmetry in the two RF currents that are used to create the double well.

Second, information about the relative coherence of the gases is obtained by matter-wave interference (Fig. 2.15). To this end, all potentials are turned off at the same time. The atoms drop and form an interference pattern after a time-of-flight expansion. As discussed in Sect. 1.5, the location of the fringes in this interference pattern is a direct measure for the relative phase between the two gases. Due to the low trapping frequency in the longitudinal direction, the expansion of the gases in this direction is negligible and the local displacement of the interference fringes indeed reflects the in situ phase distribution.

To extract the interference contrast  $C(L)$  the absorption image is summed over a length  $L$  and fitted with the cosine-modulated Gaussian function [54]

$$f_L(x) = A \cdot \exp\left(-\frac{(x - x_0)^2}{2\sigma^2}\right) \cdot \left[1 + C(L) \cos\left(\frac{2\pi(x - x_0)}{\lambda_F} + \theta(L)\right)\right], \quad (2.12)$$

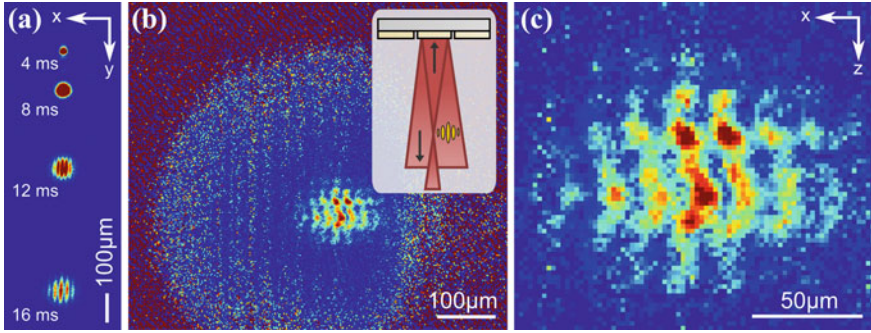


**Fig. 2.15** Matter-wave interference of two 1D Bose gases. **a** Emergence of the interference pattern in time-of-flight as seen from the longitudinal imaging system. **b** Imaging of the local fluctuations of the interference pattern using the vertical imaging system after 15.7 ms time-of-flight. The limited field of view results from the focusing of the imaging beam onto the trapping wire. The beam path is shown in the *inset* [44]. **c** Zoom into the image shown in (b). Fitting the local interference pattern allows the determination of the relative phase  $\theta(z)$  and the contrast  $C(L)$ , where  $L$  is the integration length

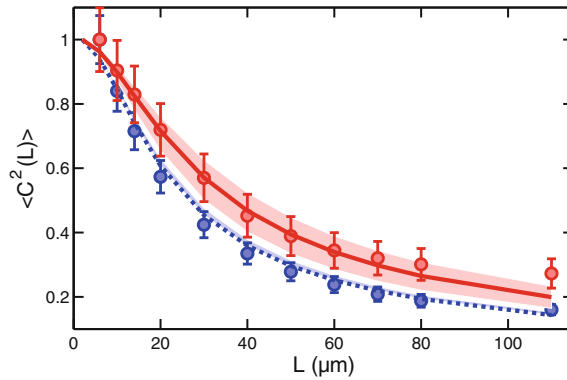


**Fig. 2.16** Decay of the mean contrast squared. *Points* represent experimental data for  $\langle C^2(L) \rangle$ , normalized to  $\langle C^2(6 \mu\text{m}) \rangle$ . *Lines* are the theory prediction (Eq. 1.87). Parameters are  $n_{1D} = 35/\mu\text{m}$ ,  $T = (27 \pm 7) \text{ nK}$  (red dashed line) and  $n_{1D} = 45/\mu\text{m}$ ,  $T = (117 \pm 7) \text{ nK}$  (blue dashed line). A bootstrapped fit of the experimental data [36, 55] is used to extract the values  $\lambda_T = (7.02 \pm 2.45) \mu\text{m}$  (red solid line) and  $\lambda_T = (2.99 \pm 0.7) \mu\text{m}$ , in good agreement with the expected 7.2 and 2  $\mu\text{m}$

where  $\sigma$  is the rms radius of the Gaussian profile,  $x_0$  is its center of mass, and  $\lambda_F$  is the fringe spacing. The results are shown in Fig. 2.16. To extract the relative phase profile  $\theta(z)$ , the integration length  $L$  is set to the size of one pixel.

To extract the FDFs, we repeat the experiment many times with the same conditions and measure the different outcomes of the contrast. Examples of measured FDFs in equilibrium are shown in Fig. 2.17. Note that this procedure is fundamentally different to the averaging performed in a 2D optical lattice. There, typically many



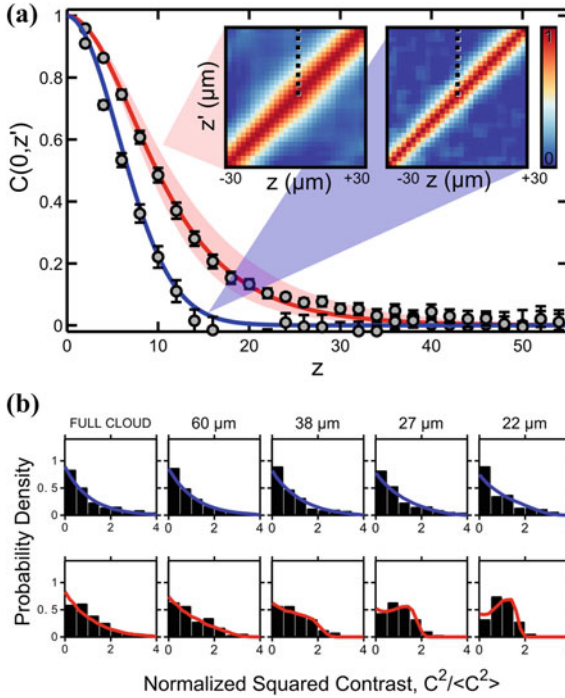


**Fig. 2.17** A pair of 1D Bose gases in thermal equilibrium. **a** Two-point phase correlation functions  $C(0, z')$  for  $n_{1D} = 35/\mu\text{m}$ ,  $T = (27 \pm 7) \text{ nK}$  (red) and for  $n_{1D} = 45/\mu\text{m}$ ,  $T = (117 \pm 7) \text{ nK}$  (blue). Solid lines denote the theory predictions (Eq. 1.85), including the optical resolution. Points are the experimental results, averaged over approximately 100 realizations. The temperatures used for the theory lines have been independently determined using density ripples, demonstrating that the gases are in equilibrium. For the hotter dataset, the correlation function is completely determined by the optical resolution. Such high-temperature datasets thus enable an independent determination of the point spread function width  $\sigma_{\text{PSF}}$  (Eq. 2.11). The insets show the corresponding full two-point correlation functions  $C(z, z')$ , with the dashed lines indicating the  $C(0, z')$  lines. **b** The corresponding FDFs are exponentially decaying on all length scales for hot temperatures and show a crossover from exponentially decaying to Gumbel-like for lower temperatures [56], both in very good agreement with theory [57, 58]. Figure (b) adapted from [44]

1D gases are realized and probed in parallel which means that only ensemble averages are available. Due to the central limit theorem the statistics of such averages is approximately Gaussian, meaning that the information contained in the higher moments of the FDFs is not accessible in this way.

As in the case of a single 1D Bose gas, we can further image the atoms transversally to extract information using the resulting density fluctuations in time-of-flight. As the two gases are completely independent, the resulting density ripple pattern is an incoherent superposition of two single density ripple patterns. We simulate this situation using the Ornstein-Uhlenbeck process technique and use it to extract a



temperature (see Sect. 1.4.6). As expected for thermal equilibrium, we find exactly the same temperature as for the anti-symmetric mode.

## References

1. T. Kinoshita, T. Wenger, D.S. Weiss, Observation of a one-dimensional Tonks-Girardeau gas. *Science* **305**, 1125–1128 (2004)
2. M. Greiner, I. Bloch, O. Mandel, T.W. Hänsch, T. Esslinger, Exploring phase coherence in a 2D lattice of Bose-Einstein condensates. *Phys. Rev. Lett.* **87**, 160405 (2001)
3. E. Haller, R. Hart, M.J. Mark, J.G. Danzl, L. Reichsollner, M. Gustavsson, M. Dalmonte, G. Pupillo, H.-C. Nagerl, Pinning quantum phase transition for a Luttinger liquid of strongly interacting bosons. *Nature* **466**, 597–600 (2010)
4. F. Serwane, G. Zürn, T. Lompe, T.B. Ottenstein, A.N. Wenz, S. Jochim, Deterministic preparation of a tunable few-Fermion system. *Science* **332**, 336 (2011)
5. P. Krüger, S. Hofferberth, I.E. Mazets, I. Lesanovsky, J. Schmiedmayer, Weakly interacting Bose gas in the one-dimensional limit. *Phys. Rev. Lett.* **105**, 265302 (2010)
6. C. Foot, *Atomic Physics* (Oxford University Press, Oxford, 2008)
7. C.V. Sukumar, D.M. Brink, Spin-flip transitions in a magnetic trap. *Phys. Rev. A* **56**, 2451–2454 (1997)
8. K.B. Davis, M.-O. Mewes, M.A. Joffe, M.R. Andrews, W. Ketterle, Evaporative cooling of sodium atoms. *Phys. Rev. Lett.* **74**, 5202 (1995)
9. W. Ketterle, D.S. Durfee, D.M. Stamper-Kurn, in *Making, Probing and Understanding Bose-Einstein Condensates*, ed. by M. Inguscio, S. Stringari, C.E. Wieman. Bose-Einstein Condensation in Atomic Gases, Proceedings of the International School of Physics Enrico Fermi (IOS Press, Amsterdam, 1999), pp. 67–176
10. W. Hänsel, P. Hommelhoff, T.W. Hänsch, J. Reichel, Bose-Einstein condensation on a micro-electronic chip. *Nature* **413**, 498–501 (2001)
11. H. Ott, J. Fortagh, G. Schlotterbeck, A. Grossmann, C. Zimmermann, Bose-Einstein condensation in a surface microtrap. *Phys. Rev. Lett.* **87**, 230401 (2001)
12. R. Folman, P. Kruger, J. Schmiedmayer, J. Denschlag, C. Henkel, Microscopic atom optics: from wires to an atom chip. *Adv. At. Mol. Opt. Phys.* **48**, 263–356 (2002)
13. J. Reichel, V. Vuletic (eds.), *Atom Chips* (Wiley-VCH, New York, 2011)
14. J. Reichel, W. Hänsel, T.W. Hänsch, Atomic micromanipulation with magnetic surface traps. *Phys. Rev. Lett.* **83**, 3398–3401 (1999)
15. T. Schumm, S. Hofferberth, L.M. Andersson, S. Wildermuth, S. Groth, I. Bar-Joseph, J. Schmiedmayer, P. Kruger, Matter-wave interferometry in a double well on an atom chip. *Nat. Phys.* **1**, 57–62 (2005)
16. M.F. Riedel, P. Böhi, Y. Li, T.W. Hänsch, A. Sinatra, P. Treutlein, Atom-chip-based generation of entanglement for quantum metrology. *Nature* **464**, 1170–1173 (2010)
17. T. Jacqmin, J. Armijo, T. Berrada, K.V. Kheruntsyan, I. Bouchoule, Sub-Poissonian fluctuations in a 1D Bose gas: from the quantum quasicondensate to the strongly interacting regime. *Phys. Rev. Lett.* **106**, 230405 (2011)
18. A.H. van Amerongen, J.J.P. van Es, P. Wicke, K.V. Kheruntsyan, N.J. van Druten, Yang-Yang thermodynamics on an atom chip. *Phys. Rev. Lett.* **100**, 090402 (2008)
19. J. Verdú, H. Zoubi, Ch. Koller, J. Majer, H. Ritsch, J. Schmiedmayer, Strong magnetic coupling of an ultracold gas to a superconducting waveguide cavity. *Phys. Rev. Lett.* **103**, 043603 (2009)
20. R. Amsüss, Ch. Koller, T. Nöbauer, S. Putz, S. Rotter, K. Sandner, S. Schneider, M. Schramböck, G. Steinhauser, H. Ritsch, J. Schmiedmayer, J. Majer, Cavity QED with magnetically coupled collective spin states. *Phys. Rev. Lett.* **107**, 060502 (2011)
21. P. Treutlein, T.W. Hänsch, J. Reichel, A. Negretti, M.A. Cirone, T. Calarco, Microwave potentials and optimal control for robust quantum gates on an atom chip. *Phys. Rev. A* **74**, 022312 (2006)

22. M. Gring, Prethermalization in an isolated many-body system. Ph.D. thesis, Vienna University of Technology, 2012
23. S. Wildermuth, P. Krüger, C. Becker, M. Brajdic, S. Haupt, A. Kasper, R. Folman, J. Schmiedmayer, Optimized magneto-optical trap for experiments with ultracold atoms near surfaces. *Phys. Rev. A* **69**, 030901 (2004)
24. O. Zobay, B.M. Garraway, Atom trapping and two-dimensional Bose-Einstein condensates in field-induced adiabatic potentials. *Phys. Rev. A* **69**, 023605 (2004)
25. Y. Colombe, E. Knyazchyan, O. Morizot, B. Mercier, V. Lorent, H. Perrin, Ultracold atoms confined in RF-induced two-dimensional trapping potentials. *Eur. Phys. Lett.* **67**, 593 (2004)
26. I. Lesanovsky, T. Schumm, S. Hofferberth, L.M. Andersson, P. Krüger, J. Schmiedmayer, Adiabatic radio frequency potentials for the coherent manipulation of matter waves. *Phys. Rev. A* **73**, 033619 (2006)
27. R. Loudon, *The Quantum Theory of Light* (Oxford University Press, Oxford, 2000)
28. S. Will, Atom optical experiments with ultracold sodium atoms. Diplomarbeit, Johannes Gutenberg-Universität Mainz, 2006
29. S. Hofferberth, Coherent manipulation of Bose-Einstein condensates with radio-frequency adiabatic potentials on atom chips. Ph.D. thesis, University of Heidelberg, 2007
30. I. Lesanovsky, S. Hofferberth, J. Schmiedmayer, P. Schmelcher, Manipulation of ultracold atoms in dressed adiabatic RF-potentials. *Phys. Rev. A* **74**, 033619 (2006)
31. M. Göbel, Low Dimensional Traps for Bose-Fermi Mixtures. Ph.D. thesis, Ruperto-Carola University of Heidelberg (2008)
32. S. Hofferberth, B. Fischer, T. Schumm, J. Schmiedmayer, I. Lesanovsky, Ultracold atoms in radio-frequency dressed potentials beyond the rotating-wave approximation. *Phys. Rev. A* **76**, 013401 (2007)
33. J.H. Shirley, Solution of the Schrödinger equation with a Hamiltonian periodic in time. *Phys. Rev.* **138**, B979–B987 (1965)
34. C. vom Hagen, Towards a low-dimensional degenerate Fermi-Fermi-Bose mixture. Ph.D. thesis, Ruperto-Carola University of Heidelberg, 2008
35. M. Kuhnert, A dual-species two-MOT setup for preparing a Bose-Fermi mixture on an atom chip. Diplomarbeit, Vienna University of Technology, 2008
36. M. Kuhnert, Thermalization and prethermalization in an ultracold Bose gas. Ph.D. thesis, Vienna University of Technology, 2013
37. T. Langen, M. Gring, M. Kuhnert, B. Rauer, R. Geiger, D. Adu Smith, I.E. Mazets, J. Schmiedmayer, Prethermalization in one-dimensional Bose gases: description by a stochastic Ornstein-Uhlenbeck process. *Eur. Phys. J. Special Topics* **217**, 43–53 (2013)
38. M. Born, E. Wolf, *Principles of Optics* (Cambridge University Press, Cambridge, 1997)
39. A. Marte, Feshbach-Resonanzen bei Stößen ultrakalter Rubidiumatome. Ph.D. thesis, Technische Universität, München, 2003
40. B. Stix, A new imaging system for dual-species atomchip experiments. Diplomarbeit, Vienna University of Technology, 2008
41. W. Alt, An objective lens for efficient fluorescence detection of single atoms. *Optik* **113**, 142 (1996)
42. T. Langen, Comment on “Probing phase fluctuations in a 2D degenerate Bose gas by free expansion”. *Phys. Rev. Lett.* **111**, 159601 (2013)
43. A. Putra, D.L. Campbell, R.M. Price, S. De, I.B. Spielman, Optimally focused cold atom systems obtained using density-density correlations. *Rev. Sci. Instrum.* **85**, 013110 (2014)
44. D. Adu Smith, M. Gring, T. Langen, M. Kuhnert, B. Rauer, R. Geiger, T. Kitagawa, I. Mazets, E. Demler, J. Schmiedmayer, Prethermalization revealed by the relaxation dynamics of full distribution functions. *New J. Phys.* **15**, 075011 (2013)
45. R. Bücker, A. Perrin, S. Manz, T. Betz, Ch. Koller, T. Plisson, J. Rottmann, T. Schumm, J. Schmiedmayer, Single-particle-sensitive imaging of freely propagating ultracold atoms. *New J. Phys.* **11**, 103039 (2009)
46. S. Dettmer, D. Hellweg, P. Ryyty, J. Arlt, W. Ertmer, K. Sengstock, D.S. Petrov, G. Shlyapnikov, H. Kreutzmann, L. Santos, M. Lewenstein, Observation of phase fluctuations in elongated Bose-Einstein condensates. *Phys. Rev. Lett.* **87**, 160406 (2001)

47. A. Imambekov, I.E. Mazets, D.S. Petrov, V. Gritsev, S. Manz, S. Hofferberth, T. Schumm, E. Demler, J. Schmiedmayer, Density ripples in expanding low-dimensional gases as a probe of correlations. *Phys. Rev. A* **80**, 033604 (2009)
48. J.-Y. Choi, S.W. Seo, W.J. Kwon, Y. Shin, Probing phase fluctuations in a 2D degenerate Bose gas by free expansion. *Phys. Rev. Lett.* **109**, 125301 (2012)
49. I.E. Mazets, Two-dimensional dynamics of expansion of a degenerate Bose gas. *Phys. Rev. A* **86**, 055603 (2012)
50. S. Manz, R. Bücke, T. Betz, Ch. Koller, S. Hofferberth, I.E. Mazets, A. Imambekov, E. Demler, A. Perrin, J. Schmiedmayer, T. Schumm, Two-point density correlations of quasicondensates in free expansion. *Phys. Rev. A* **81**, 031610 (2010)
51. T. Schumm, J. Esteve, C. Figl, J.B. Trebbia, C. Aussibal, H. Nguyen, D. Mailly, I. Bouchoule, C.I. Westbrook, A. Aspect, Atom chips in the real world: the effects of wire corrugation. *Eur. Phys. J. D* **32**, 171–180 (2005)
52. C. Menotti, S. Stringari, Collective oscillations of a one-dimensional trapped Bose-Einstein gas. *Phys. Rev. A* **66**, 043610 (2002)
53. H. Moritz, T. Stöferle, M. Köhl, T. Esslinger, Exciting collective oscillations in a trapped 1D gas. *Phys. Rev. Lett.* **91**, 250402 (2003)
54. M. Kuhnert, R. Geiger, T. Langen, M. Gring, B. Rauer, T. Kitagawa, E. Demler, D. Adu Smith, J. Schmiedmayer, Multimode dynamics and emergence of a characteristic length scale in a one-dimensional quantum system. *Phys. Rev. Lett.* **110**, 090405 (2013)
55. I. Hughes, T. Hase, *Measurements and Their Uncertainties: A Practical Guide to Modern Error Analysis* (Oxford University Press, Oxford, 2010)
56. S. Hofferberth, I. Lesanovsky, T. Schumm, A. Imambekov, V. Gritsev, E. Demler, J. Schmiedmayer, Probing quantum and thermal noise in an interacting many-body system. *Nat. Phys.* **4**, 489–495 (2008)
57. V. Gritsev, E. Altman, E. Demler, A. Polkovnikov, Full quantum distribution of contrast in interference experiments between interacting one dimensional Bose liquids. *Nat. Phys.* **2**, 705–709 (2006)
58. H.-P. Stimming, N.J. Mauser, J. Schmiedmayer, I.E. Mazets, Fluctuations and stochastic processes in one-dimensional many-body quantum systems. *Phys. Rev. Lett.* **105**, 015301 (2010)

Non-equilibrium Dynamics of One-Dimensional Bose  
Gases

Langen, T.

2015, XV, 146 p. 56 illus., 19 illus. in color., Hardcover

ISBN: 978-3-319-18563-7